ORIGINAL RESEARCH ARTICLE

Achieving High Strength and High Electrical Conductivity of Additive Manufactured CuCrZr Alloys: The Role of the Post-Heat Treatments on Microstructure and Properties

ZHANGPING HU, ZHUFENG LIU, TENG MA, ZHENGJIANG GAO, BIN GAN, ZONGQING MA, and YONGCHANG LIU

In this work, two different types of post-heat treatment processes were developed for additively manufactured CuCrZr alloy. The effect of post-heat treatment on the microstructure and properties of as-built CuCrZr alloy was studied in detail. After the direct aging of the as-built samples, the cellular substructure was preserved and a large number of fine Cu_4Zr and Cr particles were precipitated in the matrix. However, after solid solution and age-hardening treatment, the grains in the sample coarsened to hundreds of microns and the annihilation of the cellular substructure occurred. Compared with the samples after solid solution and age-hardening treatment, the directly aged samples had an excellent combination of hardness (191 ± 7 HV), strength (513 ± 8 MPa) and electrical conductivity (82.2 ± 1.5 pct IACS). The high strength of the directly aged samples can be attributed to the enhancement of the strengthening mechanism of the precipitated particles and the retention of the cellular substructure. In addition, the reduction of solid solution atoms would significantly weaken the electron scattering effect, thereby improving the electrical conductivity.

https://doi.org/10.1007/s11661-023-07165-y

I. INTRODUCTION

THE preparation of metal materials based on additive manufacturing has received extensive attention in recent years, because additive manufacturing has unique advantages in technology compared with traditional processes, such as material efficient manufacturing, low cost and the ability to prepare complex structural parts.[1–4] Specifically, laser powder bed fusion (LPBF), as a type of additive manufacturing technology, is based on the principle of layered stacking of slices and computer-aided design data of the three-dimensional digital model of the molded part. And the laser beam energy scans the metal powder in a specific area layer by layer to realize the rapid moldless near net shape manufacturing of complex structural parts.[5,6] At present, a variety of metal materials have been prepared based on LPBF technology, such as tungsten-based alloys,[7,8] 316L alloys[9] and shape-memory alloys.[10]

As a typical precipitation-strengthened alloy, CuCrZr alloy has a wide range of applications due to its excellent electrical, good machinability, excellent mechanical properties and excellent thermal conductivity, such as electronic, nuclear and aerospace industries.[11–20] A lot of research has been devoted to the preparation of defect-free copper alloys by additive manufacturing. The characteristics of high laser reflectivity, low viscosity and high thermal conductivity have brought great challenges to the preparation of CuCrZr alloy by laser additive manufacturing. In this regard, the researchers have realized the preparation of defect-free CuCrZr alloy by optimizing the LPBF process parameters. For example, Ma *et al.*[21] discussed the influence of LPBF process parameters on the microstructure of CuCrZr alloys and established a set of statistical models to analyze the relationship between processing parameters and density. On this basis, the defect-free CuCrZr alloy prepared by LPBF had a strength of 321 MPa and a ductility of 25 pct. A relative density of 94.3 pct was achieved for CuCrZr samples manufactured by LPBF with the same

ZHANGPING HU, ZHUFENG LIU, ZONGQING MA, and YONGCHANG LIU are with the State Key Lab of Hydraulic Engineering Simulation and Safety, School of Materials Science and Engineering, Tianjin University, Tianjin 300072, P.R. China. Contact e-mail: zqma@tju.edu.cn TENG MA and ZHENGJIANG GAO are with the Avimetal Powder Metallurgy Technology Co., Ltd., Beijing 100176, P.R. China. BIN GAN is with the Beijing Key Laboratory of Advanced High Temperature Materials, Central Iron and Steel Research Institute, Beijing 100081, P.R. China.
Zhangping Hu and Zhufeng Liu have contributed equally to this work.
Manuscript submitted January 12, 2023; accepted August 2, 2023.
Article published online August 16, 2023

parameters as pure Cu. The absorption coating significantly improved the relative density by 7 pct compared to the pure Cu part. Hu *et al.*[22] studied the effect of LPBF scanning parameters on the microstructure and mechanical properties of CuCrZr alloy and revealed the formation mechanism of the defect. The relative density of CuCrZr alloy prepared under the optimal process parameters reached 99.5 pct. However, the LPBF characterized by rapid melting and solidification (heat/-cool rates: ~ 10^3 to 10^8 K/s) makes the copper alloy undergo a highly non-equilibrium solidification, resulting in a unique microstructure that differs from that of copper alloys prepared by the traditional process, including cellular substructure and supersaturation solid solution.[23–25] This unique microstructure of CuCrZr prepared by LPBF brings low strength and low electrical conductivity, which cannot meet the requirements of the industrial field. Therefore, the post-heat treatment of AM-prepared metallic materials is usually required to further improve material properties through microstructural engineering. At present, a preliminary study has been carried out on the effect of post-heat treatment on the microstructure, electrical conductivity and mechanical properties of CuCrZr alloy prepared by LPBF. For example, Wallis *et al.*[26] discussed the effect of heat treatment on the microstructure and properties of CuCrZr alloys manufactured by LPBF. They pointed out that the directly aged samples had a significantly high strength of 466 MPa and thermal properties of 300 W/(m K) than that of the as-built samples. Guan *et al.*[27] analyzed the effects of laser power and scanning speed on the properties of CuCrZr alloy prepared by LPBF and studied the effect of aging temperature on the properties of the alloy. After direct aging treatment, the strength and electrical conductivity of the alloy gradually decreased and increased respectively with the increase of aging temperature. The strength and the electrical conductivity of the alloy can reach 490 MPa and 73 pct IACS (International Annealed Copper Standard, IACS) respectively after aging treatment. Wang *et al.*[28] investigated the effects of aging treatment on the microstructure, electrical conductivity and mechanical properties of CuCrZr alloys prepared by LPBF. After the aging process, the conductivity increased from 22.16 pct IACS to 72.8 pct IACS and the strength increased from 265.5 to 612.0 MPa. However, the above research lacks an in-depth study on the mechanism of microstructure evolution during heat treatment, including precipitated particles, and lacks the influence of microstructure evolution on mechanical properties and electrical conductivity. It is necessary to further elucidate the influence mechanism of the post-heat treated microstructure on the properties and to formulate a heat treatment process suitable for copper alloys prepared by LPBF to achieve simultaneous improvements in strength and electrical conductivity.

In present work, different types of heat treatment schedules have been developed for CuCrZr samples prepared by LPBF. On this basis, the mechanism of the microstructural evolution of the samples under different post-heat treatments has been investigated. The influence mechanism of the electrical conductivity and mechanical properties of the sample brought about by the difference in microstructure have been further explored. The relationship between the microstructure and properties of the sample has been established.

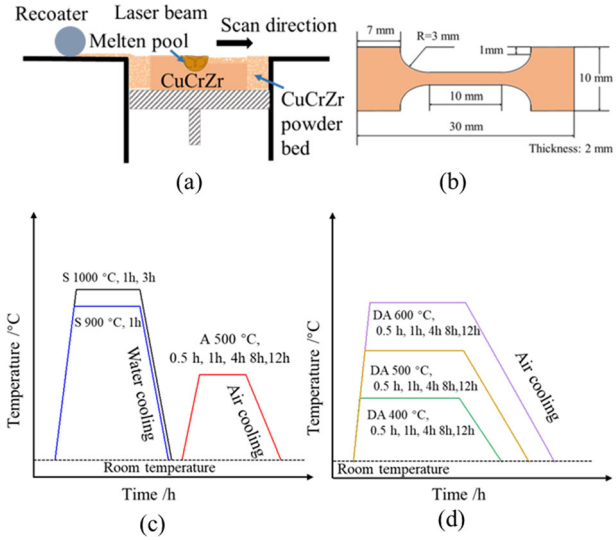

Fig. 1—(*a*) The schematic diagram of the LPBF processing. (*b*) The schematic diagram of tensile CuCrZr samples. Schematic diagram of the heat treatment process of CuCrZr sample: (*c*) Solid-solution aging and (*d*) direct aging. S stands for solid-solution treatment, A stands for aging treatment, DA stands for direct aging treatment.

II. EXPERIMENTAL

A. *The Samples Prepared by LPBF*

The gas-atomized CuCrZr powder (Cr: 0.87 wt pct, Zr: 0.12 wt pct and Cu: 99.01 wt pct) was used in the experiment. The powder was spherical particles with diameters of 15 to 53 μm. The printing of the CuCrZr parts was achieved by a Renishaw AM400 SLM device (Renishaw Plc, UK), which uses a Yb-YAG laser with a laser wavelength of 1060 nm. According to the original equipment manufacturer's instructions, the maximum power of the laser is 400 W, and the laser beam diameter is 70 μm. The CuCrZr samples were printed using the pulsed mode of the laser. The optimized printing parameters were set as 400 W laser power, 30 μm layer thickness, 90 μm hatching distance, 40 μm point distance and 200 μs exposure time. The laser volumetric energy density (E_v) can be expressed as:

$$E_v = \frac{Pt}{dHL}, \quad [1]$$

where P is the laser power, t is the exposure time, d is the point distance, H is the hatch distance and L is the layer thickness, respectively. Thus, the laser volumetric energy density for preparing CuCrZr alloy was determined to be 741 J/mm^3. The printing of the samples was carried out in a high-purity argon atmosphere (99.999 pct) to prevent oxygen contamination. The schematic diagram of CuCrZr samples prepared by LPBF is shown in Figure 1(a). The relative density of the CuCrZr part was

measured to be higher than 99.5 pct based on the Archimedes method, indicating that the sample could be subjected to subsequent testing.

B. *The Post-Heat Treatments*

As a typical class of precipitation hardening alloys, CuCrZr alloys prepared by traditional methods use two-step heat treatment schedules, including solid-solution annealing (S) and age hardening (A), to improve their properties, which is its standard heat treatment schedules for CuCrZr alloys prepared by traditional methods.[11,29–31] However, due to the characteristics of high heating/cooling rate and intrinsic heat treatment effect of LPBF, the direct age hardening heat treatment schedule needs to be considered for the CuCrZr alloy prepared by LPBF. Therefore, two heat treatment schedules, solid-solution aging (SA) and direct aging (DA), were carried out on the CuCrZr alloy prepared by LPBF to study the difference in the microstructure and properties. The heat treatment parameters of solid-solution aging and direct aging are shown in Figures 1(c) and (d), respectively.

C. *Samples Characterization*

CuCrZr samples with a size of $8 \times 8 \times 8$ mm^3 under different heat treatment conditions were ground sequentially with 400 to 7000 mesh sandpaper, and then polished with a diamond suspension with a particle size of 2.5 μm on a polishing machine equipped with flannelette. The hardness of CuCrZr samples under different heat treatment conditions was measured by a Vickers hardness tester with a load of 0.2 kg for 10 seconds. The electrical conductivity of the polished CuCrZr samples with a size of $12 \times 12 \times 5$ mm^3 under different heat treatment conditions was measured using an eddy current conductometer. Six areas per sample were measured and averaged. The polished surface of the CuCrZr samples under different heat treatment conditions was etched with a reagent for 8 seconds (30 mL deionized water, 1.5 g $FeCl_3$ and 15 mL HCl) to highlight the microstructure. The microstructural characterization of the samples was carried out by optical microscope (OM) and scanning electron microscopy (SEM, JEOL JSM-7800F) equipped with integrated Electron Backscatter Diffraction (EBSD). The samples for EBSD analysis were prepared by electropolishing with an electrolyte containing a mixture of 100 mL phosphoric acid, 150 mL ethanol and 250 mL deionized water. The EBSD images of the as-built sample, DA sample and SA sample were obtained at magnifications of 150, 150 and 50, respectively. The detailed microstructural characterization of samples was carried out using a JEOL JEM-2100F transmission electron microscope (TEM) operated at an acceleration voltage of 200 kV and equipped with a JED-2300T EDAX energy-dispersive X-ray spectroscopy (EDS) detector, which is a windowless electric refrigerated spectroscopy probe. The samples for TEM analysis were mechanically ground to 25 μm and then double jet thinned using a 25 pct nitric acid in methanol solution at − 30 °C to obtain a suitable thin area. The tensile test of the sample was carried out at room temperature under quasi-static loading using an MTS CMT-5105 universal tensile testing machine. The bone-like tensile samples used for testing have a gauge length of 10 mm, as shown in Figure 1(b). Three independent tensile tests were performed on samples of each heat treatment condition.

III. RESULTS AND DISCUSSION

A. *The Hardness and Electrical Conductivity Analysis of CuCrZr Samples*

The hardness and electrical conductivity, two key properties of age-hardening copper alloy properties, were used to evaluate heat treatments. Figure 2 shows the hardness and electrical conductivity of the samples under different heat treatment conditions. The hardness value of the as-built sample was determined to be 83 ± 5 HV. For the hardness of the CuCrZr alloy adopting the solution aging heat treatment scheme, it can be seen that when the solid-solution temperature is 950 °C or 1000 °C, the hardness of the sample was about 65 HV. During the subsequent aging process, the hardness of solid-solution samples at 950 °C or 1000 °C decreased with the prolongation of aging time, and the solid-solution sample after aging for 0.5 hour had the highest hardness. Compared with other solution-aged samples, the samples aged at 500 °C for 0.5 hour after solution treated at 1000 °C for 1 hour had the highest hardness of 130 ± 6 HV. For the hardness of the CuCrZr alloy using the direct aging hardening heat treatment scheme, the hardness of the samples aged at 500 °C and 600 °C gradually decreased with the progress of aging. Among the samples treated with direct aging hardening, the samples aged at 500 °C for 0.5 hour had the highest hardness of about 191 ± 7 HV, which indicates that the peak aging has been reached. The electrical conductivity of the samples under different conditions is shown in Figure 2(b). The as-built sample had the lowest electrical conductivity, about 20.3 ± 0.3 pct IACS. The electrical conductivity of the solution-aged samples reached about 86 pct IACS. The samples treated by direct aging at 400 °C had a low electrical conductivity of 31.8 ± 1.2 pct IACS. While the samples treated with direct aging at 500 °C and 600 °C had a high electrical conductivity of 82.2 ± 1.5 pct IACS and 82.6 ± 1.3 pct IACS, respectively. The electrical conductivities of both the directly aged (500 °C and 600 °C) and solution-aged samples are higher than the electrical conductivity standard (80 pct IACS) of CuCrZr alloy. The mechanism of the electrical conductivity of the samples under different conditions will be discussed in the next section. After evaluating the above results, the heat treatment process parameters with high electrical conductivity and high hardness were selected in both SA and DA heat treatment schemes to study the microstructure and properties of the corresponding samples and compare them with as-built CuCrZr samples. Accordingly, the as-built samples, the samples aged at 500 °C for 0.5 hour after solution aging at 1000 °C for 1 hour (SA) and the samples aged at 500 °C for 0.5 hour (DA) were selected.

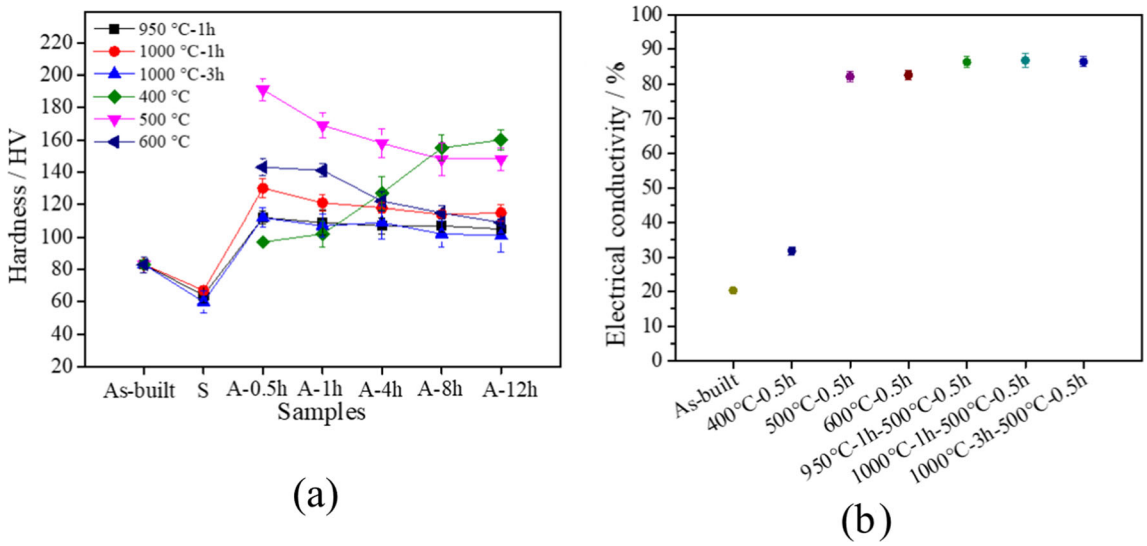

Fig. 2—(*a*) The hardness values and (*b*) electrical conductivity of as-built samples and heat-treated samples under different conditions.

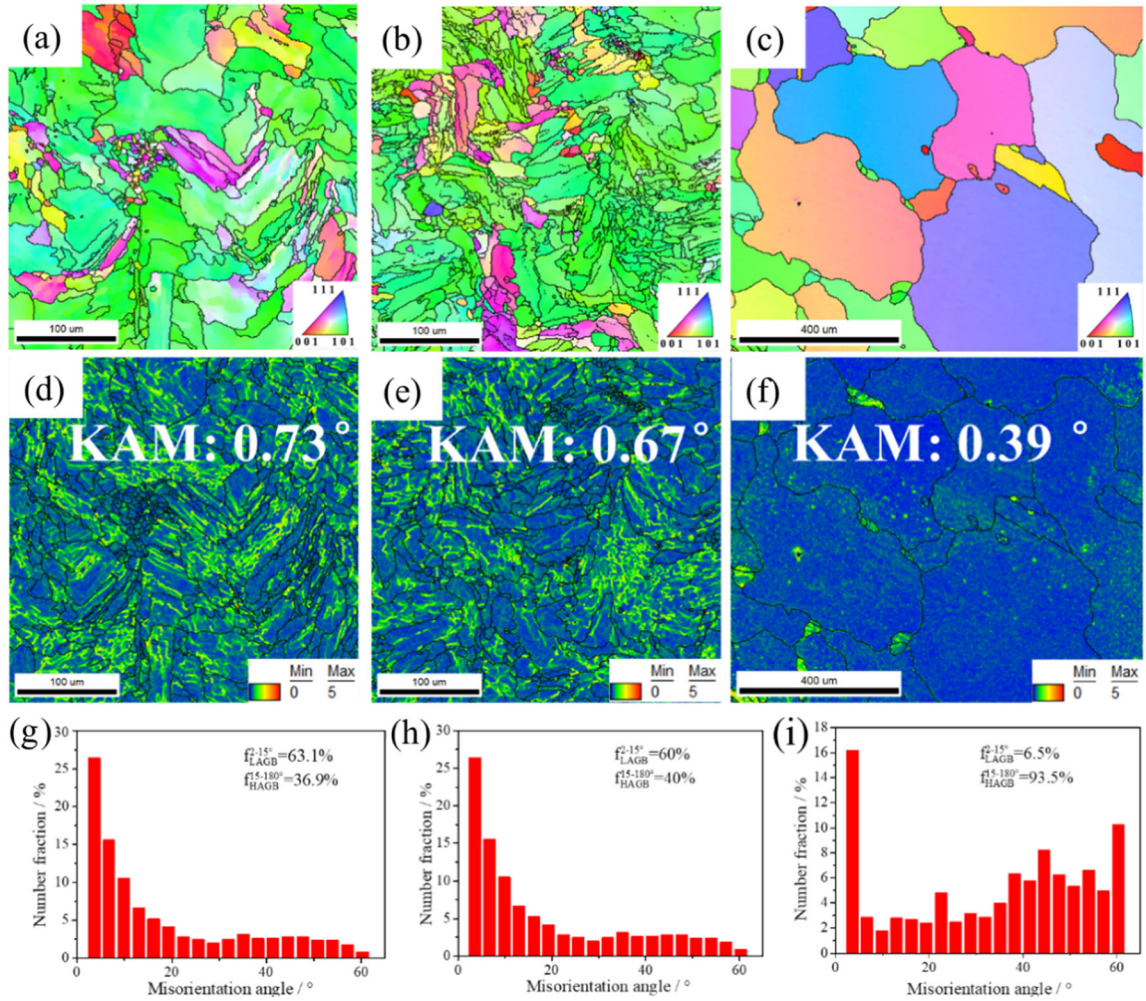

Fig. 3—The IPF image of the CuCrZr samples under different conditions: (*a*) as-built, (*b*) DA and (*c*) SA. The KAM results of the CuCrZr samples under different conditions: (*d*) as-built, (*e*) DA and (*f*) SA. The misorientation angle distribution of the CuCrZr samples under different conditions: (*g*) as-built, (*h*) DA and (*i*) SA.

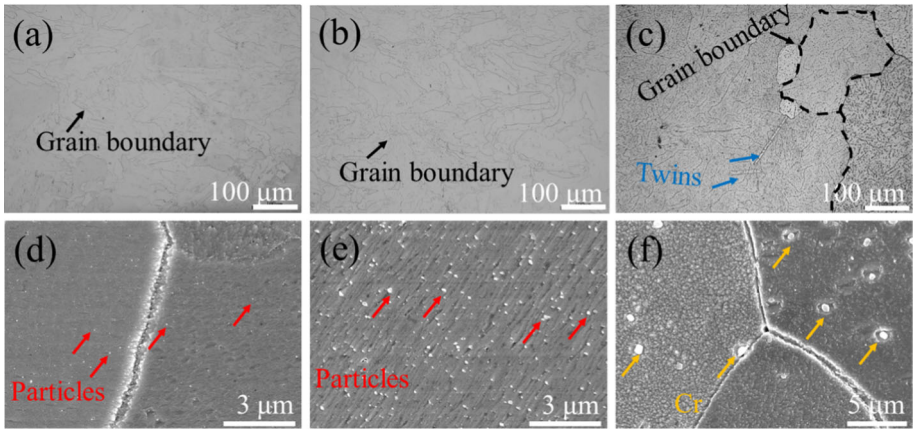

Fig. 4—The images of the CuCrZr samples under different conditions: (*a*, *d*) as-built, (*b*, *e*) DA and (*c*, *f*) SA (Color figure online).

B. *The Microstructural Evolution of CuCrZr Samples During Heat Treatment*

The EBSD characterization of as-built, DA and SA samples is shown in Figure 3. Both the as-built and DA samples exhibited irregular grains with an average size of approximately 20 μm. However, abnormal grain growth can be observed in the SA sample. The sample possesses both coarse grains and fine grains, and their average sizes were ~ 300 and ~ 20 μm, respectively. In addition, the micron-sized twins were observed in the SA sample. The degree of plastic deformation homogenization of the sample can be qualitatively reflected by the kernel average misorientation (KAM) value, which characterizes the geometric dislocation density and judges the state of the stress distribution.[32] The KAM values of the as-built, DA and SA samples were determined to be 0.73, 0.67 and 0.39, respectively. The high cooling rate and uneven heating/cooling of the LPBF results in high stresses in the as-built samples, which are relieved after the aging treatment. Therefore, the DA samples have lower KAM values compared to that of the as-built sample. This indicates that the residual stresses in the samples gradually decrease as the heat treatment proceeds. The strain distribution in the as-built and SA samples is not uniform, including high-strain regions and low-strain regions, as shown in Figures 3(d) and (e). The strain distribution of these fine grains with high KAM value is much higher than that of the coarse grains with low KAM value, as shown in Figure 3(f). The high-angle grain boundaries (HAGB) fraction of the as-built, DA and SA samples were determined to be 36.9, 40 and 93.5 pct, respectively. The HAGB fraction of the SA sample is significantly higher than that of the as-built and DA samples. The microstructure of the as-built, DA and SA samples are shown in Figure 4. A significantly larger number of fine precipitated particles (marked by red arrows) were observed in the DA sample than that of the as-built sample. Large-size Cr particles of 50 μm were observed in the SA sample, which is much larger than that of the as-built and DA samples.

The detailed microstructure of as-built, DA and SA samples was carried out by the TEM analysis, as shown in Figures 5 and 6. The cellular substructure and a large

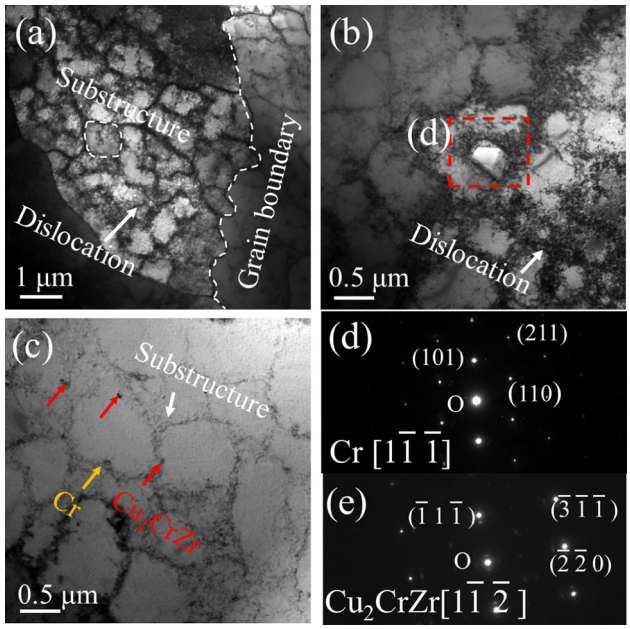

Fig. 5—TEM characterization of CuCrZr samples prepared by LPBF. (*a*, through *c*) The bright field TEM images of as-printed CuCrZr samples. (*d*) The selected area electron diffraction (SAED) pattern of precipitate in the red circles in (b). (*e*) The SAED pattern of precipitate marked by the red arrow in (c) (Color figure online).

number of dislocations decorated along the cell boundary were observed in the as-built samples, as shown in Figures 5(a) and (b), respectively, which is the common microstructure for the LPBF prepared alloy samples.[9] Localized heating/cooling-induced compression-tension cycles provided by LPBF lead to the formation of cellular dislocations.[25] The rod-like precipitates with a size of ~ 100 to 600 nm were observed in the as-built samples, which can be determined to be Cr with a BCC structure, as shown in Figures 5(b) and (d). In addition, fine particles were observed at the boundary of the cellular substructure with a size of ~ 30 to 50 nm, as shown in Figure 5(c). It was determined that two types of particles were formed at the boundary of the cellular substructure, namely Cr phase and Cu_2CrZr phase. This

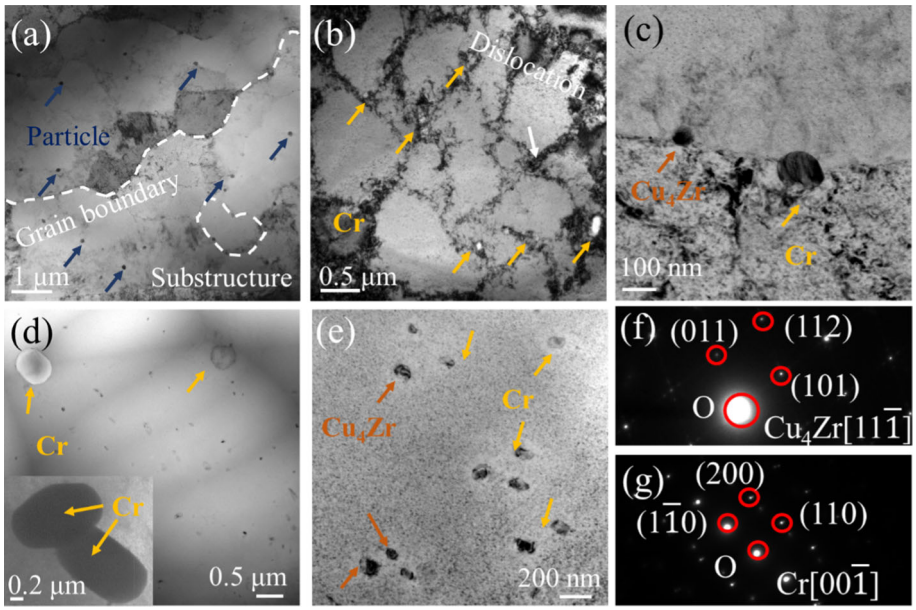

Fig. 6—TEM characterization of CuCrZr samples prepared by LPBF under different treatment states. (*a* through *c*) The bright field TEM images of DA samples, (*d* and *e*) the bright field TEM images of SA samples, the (*f*) SAED pattern of precipitates marked by the orange arrow, the (*g*) SAED pattern of precipitates marked by the yellow arrow (Color figure online).

is in line with the results of previous studies about CuCrZr samples manufactured by LPBF.[23] However, the different chemical composition of the powder result in the formation of a different phase from that in CuCrZr prepared by Salvan *et al.*[24] During the rapid melting/solidification process provided by LPBF (heat/-cool rates: ~ 10^3 to 10^8 K/s), a large-sized Cr phase (primary Cr phase) would form in the as-built samples due to the low solubility of Cr in the Cu matrix (the limit solid solubility of Cr in Cu is ~ 0.7 wt pct). In addition, when the laser is applied to the next few powder layers, it would have a rapid and short-term remelting and/or cyclic reheating on the solidified layer, which is equivalent to the "intrinsic heat treatment" effect (IHT).[33]

Figure 6 illustrates the TEM image of DA and SA samples. Cellular substructures, dislocations decorated along the cell boundary and rod-like Cr precipitates were observed in the DA sample, which was the same as in the as-built sample. The average size of the rod-like Cr precipitation particle was determined to be ~ 100 to 600 nm, as shown in Figure 6(b). A large number of fine particles were distributed at the substructure boundaries, as shown in Figure 6(a). It can be determined that the volumetric fraction of the precipitation particle in the DA sample (~ 4.5 vol pct) is much higher than that of the as-built sample (~ 2.2 vol pct). Two types of nano-particles were formed, namely Cr phase with a size of ~ 150 nm and Cu_4Zr phase with a size of ~ 20 to 50 nm. Unlike as-built samples and DA samples, no cellular substructures and dislocations were observed in SA samples. In addition to the observation of the Cu_4Zr and Cr particles with a size of ~ 80 to 150 nm, significantly coarsened Cr particles were also observed in SA samples, reaching ~ 1.5 μm in size, which is much larger than that of the as-built and DA samples. No Cu_2CrZr particles were observed in either the DA or the SA sample, which is different from that of the as-built sample.

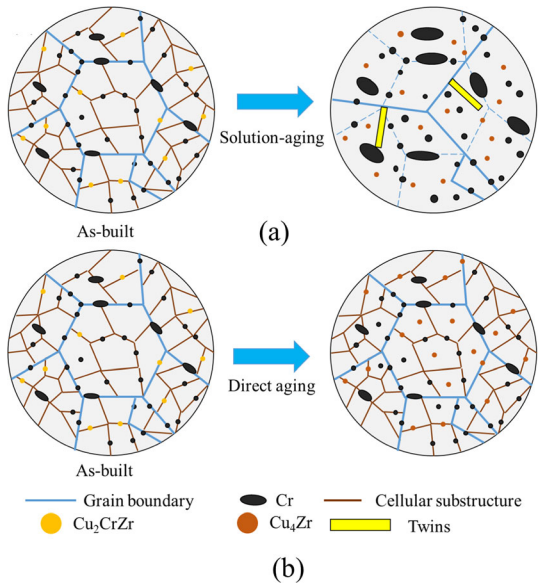

Fig. 7—Schematic diagram of microstructure evolution of as-built CuCrZr samples under different heat treatment schedules: (*a*) solid-solution aging and (*b*) direct aging.

Due to the remarkable microstructural differences in the as-built, DA and SA samples, it is necessary to discuss the evolution mechanism of the microstructure. Figure 7 shows the schematic diagram of the microstructure evolution of as-built CuCrZr samples under direct aging and solid-solution aging treatments. The grain growth of the as-built sample during the solid solution and the aging process is mainly due to the grain boundary migration mechanism.[34,35] Rearrangement

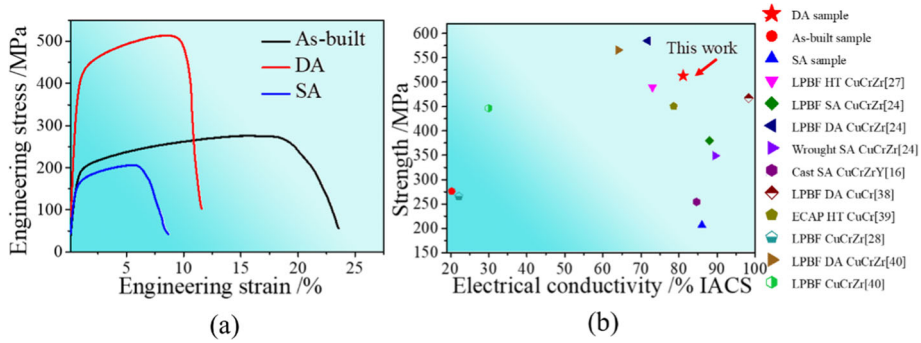

Fig. 8—(*a*) The tensile stress-strain curves of as-built, DA and SA CuCrZr samples. (*b*) A comparison between the mechanical properties of the samples in this work and other Cu alloys.

or cancellation of dislocations occurs during grain boundary migration, resulting in the annihilation of the cellular substructure. Thus, there are obvious coarse grains and no cellular dislocations in the solid-solution aging samples. Under the action of high cooling rate ($\sim 10^3$ to 10^8 K/s) and cyclic heating (IHT effect) of LPBF, the CuCrZr sample is under-aged, that is, the primary Cr phase and Cu_2CrZr phase are formed. The formation mechanism of precipitated phases in the solution-aged samples can be summarized as follows. The Cr particles and Cu_2CrZr particles in the as-built CuCrZr sample would gradually dissolve in the Cu matrix during the solid-solution process and form a supersaturated solid solution. During the subsequent aging process, the diffusion and segregation of elements in the supersaturated solid solution would lead to the coarsening of the undissolved primary Cr phase, which promotes the formation of the small-sized secondary Cr phase and Cu_4Zr phase.[23,36,37] The formation mechanism of the precipitated phase in the directly aged samples can be summarized as follows. The Cu_2CrZr particles in the as-built CuCrZr sample decompose into Cu_4Zr phase during the direct aging process. And the precipitation and diffusion of Cr elements in the solid solution lead to the formation of small-sized Cr particles and the coarsening of primary Cr particles.[23] However, there is a cellular substructure in the directly aged sample, which makes elements precipitate on the boundary of the cellular substructure, thus ensuring that the particle size of the Cr phase in the DA sample is smaller than that of the SA sample.

C. *The Properties of CuCrZr Under Different Treatment States*

Figure 8 presents the tensile stress-strain curves of as-built, DA and SA samples. The ultimate tensile strength and elongation of the as-built samples were 276 ± 6 MPa and 23.5 ± 0.5 pct, respectively. The strength of the sample after direct aging treatment reached 513 MPa and its elongation was 11.5 ± 0.8 pct. However, the strength of the solution-aged sample dropped sharply to 206 MPa and its elongation was 8.6 ± 0.5 pct, which was much lower than that of the as-built and DA samples. Therefore, the samples prepared by LPBF have the highest strength after direct aging treatment, which is better than that of additively manufactured Cu alloys after heat treatment reported in the literature,[16,24,27,28,38–40] as shown in Figure 8(b). Based on the electrical conductivity results above, the DA sample possess the best combination of strength and electrical conductivity compared to that of other samples.

The difference in the microstructure of the samples under different heat treatment states caused the difference in the electron scattering effect, which led to the different electrical conductivity of the samples.[27,41] In general, the electrical resistivity (ρ) of CuCrZr alloys can be expressed based on the following Matthiessen's rule[14]:

$$\rho = \rho_{Cu} + \Delta\rho_s + \Delta\rho_d + \Delta\rho_{gb}, \qquad [2]$$

where ρ_{Cu} are the electrical resistivity of the ideally pure Cu, which is only temperature-dependent. $\Delta\rho_s$, $\Delta\rho_d$ and $\Delta\rho_{gb}$ are the residual electrical resistivity caused by solid solution atoms, dislocation and grain boundary in the matrix, respectively. Compared with crystal defects such as dislocations and grain boundaries, the solid solution atoms in the matrix have a more significant effect on the electrical conductivity of the sample.[36,42,43] Since the grain size in all samples is on the order of micrometers, the effect of grain boundaries on electrical conductivity can be negligible. The as-built CuCrZr sample has a high density of dislocations and is in a saturated solid solution state, which means that there is a large amount of lattice distortion (dislocation and solid solution atoms) in the sample, which increases the $\Delta\rho_s$ and $\Delta\rho_d$, enhances the electron scattering effect and greatly reduces the electrical conductivity of the sample.[24,27,28] For the solid-solution aging sample, there is no large number of cellular dislocations, and the particles in the Cu matrix are fully precipitated, which decreases the values of $\Delta\rho_s$ and $\Delta\rho_d$. This indicates that the degree of lattice distortion in the sample is significantly reduced, the electron scattering effect is weakened, and the electrical conductivity of the sample is effectively improved. For the direct aging sample, there are a large number of cellular dislocations and the particles in the Cu matrix are fully precipitated, which reduces the value of $\Delta\rho_s$ but maintains the value of $\Delta\rho_d$. Therefore,

compared with the SA sample, the DA sample has lower electrical conductivity due to the high density of dislocations.

The evolution of the mechanical properties of the samples under different states can be explained by the strengthening and/or weakening mechanisms based on the microstructural differences. The high-density cellular dislocations brought about by localized heating/cooling-induced compression-tension cycles can act as a stable "regulator" during the entire plastic deformation process, hindering the movement of dislocations to improve their strength, while allowing dislocations to pass through to ensure that the entire plastic deformation process continuous plastic flow, thus ensuring its ductility.[9,44] Although the cellular dislocation substructure exists in both the as-built and the DA samples, the DA sample has a higher number of nanoparticles, which will enhance the precipitation strengthening mechanism.[45,46] A larger number of nanoparticles is more likely to hinder the movement of dislocations during plastic deformation, which will greatly improve the strength of the sample.[47] However, strain localization would occur near the nanoparticles, resulting in a decrease in the ductility of the sample.[48,49] Therefore, the DA sample has higher strength and lower ductility than that of the as-built samples. Compared with the as-built and DA sample with cellular substructure, the annihilation of the cellular substructure in the SA sample would lead to a decrease in both strength and ductility. In addition, significantly coarsened grains and precipitated particles would further reduce the strength of the sample.[50,51] The formation of the micron-sized precipitated particles would act as stress concentration points during plastic deformation, which would significantly reduce the ductility of the sample. Thus, the strength and ductility of the SA samples are lower than that of the as-built and the DA sample.

IV. CONCLUSION

In this study, two types of heat treatment schedules, including direct aging and solution aging, were developed for the CuCrZr alloy prepared by LPBF. The samples after direct aging treatment not only maintained the same cellular substructure as the as-built samples but also precipitated a larger number of nanoparticles than that of as-built samples. However, the annihilation of the cellular substructure was not only observed in the samples after solution aging treatment, but also the grains and precipitated particles were significantly coarsened. The sample after direct aging treatment possesses the best combination of hardness (191 ± 7 HV), strength (513 ± 8 MPa) and electrical conductivity (82.2 ± 1.5 pct IACS) compared to that of other samples. The high electrical conductivity of the samples after direct aging treatment can be attributed to the reduction of the electron scattering effect brought about by the precipitation of particles in the matrix. The high strength of the sample after direct aging treatment is caused by the enhancement of the strengthening mechanism of the precipitated particles and the retention of the cellular substructure. Our work provides a new heat-treatment strategy and insight into the realization of additively manufactured copper alloys with high strength and electrical conductivity.

ACKNOWLEDGMENTS

The authors are grateful to the National Natural Science Foundation of China (Grant No. U22A20172 and 52171044), the Science Foundation for Distinguished Young Scholars in Tianjin (No. 19JCJQJC61700) and the Seed Foundation of Tianjin University (Grant No. 2023XZL-0015).

COMPETING INTERESTS

The authors declare that they have no known competing financial interests or personal relationships that could have appeared to influence the work reported in this paper.

REFERENCES

1. M. Askari, D.A. Hutchins, P.J. Thomas, L. Astolfi, R.L. Watson, M. Abdi, M. Ricci, S. Laureti, L. Nie, S. Freear, R. Wildman, C. Tuck, M. Clarke, E. Woods, and A.T. Clare: *Addit. Manuf.*, 2020, vol. 36, 101562.
2. T. DebRoy, H.L. Wei, J.S. Zuback, T. Mukherjee, J.W. Elmer, J.O. Milewski, A.M. Beese, A. Wilson-Heid, A. De, and W. Zhang: *Prog. Mater Sci.*, 2018, vol. 92, pp. 112–24.
3. D. Herzog, V. Seyda, E. Wycisk, and C. Emmelmann: *Acta Mater.*, 2016, vol. 117, pp. 371–92.
4. Y.-L. Kuo, A. Kamigaichi, and K. Kakehi: *Metall. Mater. Trans. A*, 2018, vol. 49A, pp. 3831–37.
5. A.A. Martin, N.P. Calta, S.A. Khairallah, J. Wang, P.J. Depond, A.Y. Fong, V. Thampy, G.M. Guss, A.M. Kiss, K.H. Stone, C.J. Tassone, J.N. Weker, M.F. Toney, T. van Buuren, and M.J. Matthews: *Nat. Commun.*, 2019, vol. 10, p. 1987.
6. X. Guan and Y.F. Zhao: *Int. J. Adv. Manuf. Technol.*, 2020, vol. 107, pp. 1959–82.
7. Hu. Zhangping, Y. Zhao, K. Guan, Z. Wang, and Z. Ma: *Addit. Manuf.*, 2020, vol. 36, 101579.
8. Hu. Zhangping, Ye. Liu, Z. Qian, Y. Zhao, Ji. Dong, Z. Yang, Z. Wang, and Z. Ma: *Mater. Sci. Eng. A*, 2021, vol. 817, 141417.
9. Hu. Zhangping, K. Guan, Z. Qian, Ji. Dong, Wu. Jin, and Z. Ma: *J. Alloys Compd.*, 2022, vol. 899, 163262.
10. T. Gustmann, A. Neves, U. Kühn, P. Gargarella, C.S. Kiminami, C. Bolfarini, J. Eckert, and S. Pauly: *Addit. Manuf.*, 2016, vol. 11, pp. 23–31.
11. A.H. Huang, Y.F. Wang, M.S. Wang, L.Y. Song, Y.S. Li, L. Gao, C.X. Huang, and Y.T. Zhu: *Mater. Sci. Eng. A*, 2019, vol. 746, pp. 211–16.
12. J.B. Correia, H.A. Davies, and C.M. Sellars: *Acta Mater.*, 1997, vol. 45, pp. 177–90.
13. Fu. Shaoli, P. Liu, X. Chen, H. Zhou, F. Ma, W. Li, and Ke. Zhang: *Mater. Sci. Eng. A*, 2021, vol. 802, 140598.
14. D.P. Shen, N. Xu, M.Y. Gong, P. Li, H.B. Zhou, W.P. Tong, and G. Wilde: *J. Mater. Sci.*, 2020, vol. 55, pp. 12499–2512.
15. Yi. Zhang, A.A. Volinsky, H.T. Tran, Z. Chai, P. Liu, B. Tian, and Y. Liu: *Mater. Sci. Eng. A*, 2016, vol. 650, pp. 248–53.
16. D. Zhu, M. Peng, Y. Zhong, Z. Shen, T. Zheng, H. Wang, W. Ren, J. Wang, C. Li, and Z. Ren: *Mater. Res. Express*, 2018, vol. 5, 116505.

17. Hu. Jingyuan, Y. Tian, Yu. Haowei, G. Ling, S. Li, M. Jiang, H. Li, and G. Qin: *Mater. Lett*., 2022, vol. 315, 131937.
18. R. Bheekya Naik, K. Venkateswara Reddy, G. Madhusudhan Reddy, and R. Arockia Kumar: *Fusion Eng. Des*., 2020, vol. 161, p. 111962.
19. K. Jha, P. Sahlot, A.K. Singh, S. Kumar, A. Arora, R.N. Singh, and G.K. Dey: *Metall. Mater. Trans. A*, 2021, vol. 52A, pp. 680–90.
20. K. Jha, S. Kumar, K. Nachiket, K. Bhanumurthy, and G.K. Dey: *Metall. Mater. Trans. A*, 2018, vol. 49A, pp. 223–34.
21. Z. Ma, K. Zhang, Z. Ren, D.Z. Zhang, G. Tao, and Xu. Haisheng: *J. Alloys Compd*., 2020, vol. 828, 154350.
22. Z. Hu, Z. Du, Z. Yang, L. Yu, and Z. Ma: *Mater. Sci. Eng. A*, 2022, vol. 836, p. 142740.
23. Hu. Zhangping, B. Gan, J. Tan, Wu. Jin, S. Chen, Ji. Dong, and Z. Ma: *J. Alloys Compd*., 2022, vol. 927, 167111.
24. C. Salvan, L. Briottet, T. Baffie, L. Guetaz, and C. Flament: *Mater. Sci. Eng. A*, 2021, vol. 826, 141915.
25. Ge. Wang, H. Ouyang, C. Fan, Q. Guo, Z. Li, W. Yan, and Z. Li: *Mater. Res. Lett*., 2020, vol. 8, pp. 283–90.
26. C. Wallis and B. Buchmayr: *Mater. Sci. Eng. A*, 2019, vol. 744, pp. 215–23.
27. P. Guan, X. Chen, P. Liu, F. Sun, C. Zhu, H. Zhou, S. Fu, Z. Wu, and Y. Zhu: *Mater. Res. Express*, 2019, vol. 6, p. 1165c1.
28. Q. Wang, Y. Zhang, K. Wang, S. Liu, Xi. Zhang, and H. Shao: *Mater. Sci. Eng. A*, 2022, vol. 857, 144054.
29. G. Purcek, H. Yanar, M. Demirtas, Y. Alemdag, D.V. Shangina, and S.V. Dobatkin: *Mater. Sci. Eng. A*, 2016, vol. 649, pp. 114–22.
30. M. Kulczyk, W. Pachla, J. Godek, J. Smalc-Koziorowska, J. Skiba, S. Przybysz, M. Wróblewska, and M. Przybysz: *Mater. Sci. Eng. A*, 2018, vol. 724, pp. 45–52.
31. M. Kermajani, Sh. Raygan, K. Hanayi, and H. Ghaffari: *Mater. Des*., 2013, vol. 51, pp. 688–94.
32. Y. Jiang, C. Li, X. Di, D. Wang, and J. Liu: *Weld. World*, 2020, vol. 64, pp. 1213–25.
33. J. Zhang, Y. Liu, M. Bayat, Q. Tan, Y. Yin, Z. Fan, S. Liu, J.H. Hattel, M. Dargusch, and M.-X. Zhang: *Scr. Mater*., 2021, vol. 191, pp. 155–60.
34. K. Chen, H. Li, C.H. Lim, N. Jia, and W. Yan: *Scr. Mater*., 2022, vol. 219, p. 114882.
35. K. Chen, D.J. Huang, H. Li, N. Jia, and W. Chong: *Scr. Mater*., 2022, vol. 209, p. 114377.
36. C. Jinshui, Y. Bin, W. Junfeng, X. Xiangpeng, C. Huiming, and W. Hang: *Mater. Res. Express*, 2018, vol. 5, 026515.
37. E. Batawi, D.G. Morris, and M.A. Morris: *Mater. Sci. Technol*., 1990, vol. 6, pp. 892–99.
38. S. Zhang, H. Zhu, L. Zhang, W. Zhang, H. Yang, and X. Zeng: *Mater. Lett*., 2019, vol. 237, pp. 306–09.
39. C.Z. Xu, Q.J. Wang, M.S. Zheng, J.W. Zhu, J.D. Li, M.Q. Huang, Q.M. Jia, and Z.Z. Du: *Mater. Sci. Eng. A*, 2007, vol. 459, pp. 303–08.
40. X. Tang, X. Chen, F. Sun, L. Li, P. Liu, H. Zhou, Fu. Shaoli, and A. Li: *J. Alloys Compd*., 2022, vol. 924, 166627.
41. A.D. Ivanov, A.K. Nikolaev, G.M. Kalinin, and M.E. Rodin: *J. Nucl. Mater*., 2002, vol. 307–311, pp. 673–76.
42. D.P. Shen, Y.J. Zhu, X. Yang, and W.P. Tong: *Vacuum*, 2018, vol. 149, pp. 207–13.
43. S. Zhang, H. Zhu, L. Zhang, W. Zhang, H. Yang, and X. Zeng: *J. Alloys Compd*., 2019, vol. 800, pp. 286–93.
44. L. Liu, Q. Ding, Y. Zhong, Ji. Zou, Wu. Jing, Y.-L. Chiu, J. Li, Ze. Zhang, Yu. Qian, and Z. Shen: *Mater. Today*, 2018, vol. 21, pp. 354–61.
45. C. Han, R. Babicheva, J.D.Q. Chua, U. Ramamurty, S.B. Tor, C.-N. Sun, and K. Zhou: *Addit. Manuf*., 2020, vol. 36, p. 101466.
46. P. Xiao, Y. Gao, C. Yang, Y. Li, X. Huang, Q. Liu, S. Zhao, Xu. Feixing, and M. Gupta: *Composites B*, 2020, vol. 198, 108174.
47. W.H. Yu, S.L. Sing, C.K. Chua, C.N. Kuo, and X.L. Tian: *Prog. Mater. Sci*., 2019, vol. 104, pp. 330–79.
48. H. Yang, K. Li, Bu. Yeqiang, Wu. Jinming, Y. Fang, L. Meng, J. Liu, and H. Wang: *Scr. Mater*., 2021, vol. 195, 113741.
49. K. Lu: *Science*, 2010, vol. 328, pp. 319–20.
50. Y. Hong, C. Zhou, Y. Zheng, L. Zhang, J. Zheng, X. Chen, and B. An: *Mater. Sci. Eng. A*, 2019, vol. 740–741, pp. 420–26.
51. A. Mortensen and J. Llorca: *Annu. Rev. Mater. Res*., 2010, vol. 40, pp. 243–70.